2. Leichner PK, Klein JL, Garrison JB, et al. Dosimetry of I131-labeled antiferritin in hepatoma: A model for radioimmunoglobulin dosimetry. *Int J Radiat Oncol Biol Phys* 1981;7:323–333.

3. Moldofsky PJ, Beardsley MR, Mulhern Jr CB. External imaging techniques for quantitation of distribution of I-131 F(ab')$_2$ fragments of monoclonal antibody in humans. *Med Phys* 1984;11:778–783.

4. Zanzonico PB, Bigler RE, Sgouros G, Strauss A. Quantitative SPECT in radiation dosimetry. *Semin Nucl Med* 1989;19:47–61.

5. Chang LT. A method for attenuation correction in radionuclide computer tomography. *IEEE Trans Nucl Sci* 1978;NS25:638–643.

6. Jaszczak RJ, Greer KL, Coleman RE. SPECT. In: Rao DV, Chandra R, Graham MC, eds. *Physics of nuclear medicine: recent advances, medical physics monograph no. 10*, New York: American Association of Physicists in Medicine; 1984:457–482.

7. Hawkins WG, Leichner PK, Yang N-C. The circular harmonic transform for SPECT reconstruction and boundary conditions on the Fourier transform of the sinogram. *IEEE Trans on Med Imaging* 1988;7:135–148.

8. Weber DA, Eckerman KF, Dillman LT, Ryman JC. *MIRD: radionuclide data and decay schemes*. New York: Society of Nuclear Medicine; 1989.

9. Frey P, Townsend O, Jeavons A, Donath A. In vivo imaging of the human thyroid with a positron camera using I-124. *Eur J Nucl Med* 1985;10:472–476.

10. Miraldi F, Nelson AD, Berridge MS, Cheung N-KV. Positron imaging of neuroblastoma tumors with $^{124}I/^{123}I$-labeled monoclonal antibody 3F8 [Abstract]. *J Nucl Med* 1987;28:1078.

11. Ott RJ, Batty V, Webb S, et al. Measurement of radiation dose to the thyroid using positron emission tomography. *Br J Radiol* 1987;60:245–251.

12. Lambrecht RM, Woodhouse N, Phillips R, et al. Investigational study of iodine-124 with a positron camera. *Am J Physiol Imaging* 1988;3:197–200.

13. Miraldi F. Monoclonal antibodies and neuroblastoma. *Semin Nucl Med* 1989;19:282–294.

14. Langen K-J, Coenen HH, Rosen N, et al. SPECT studies of brain tumors with L-3-[^{123}I]iodo-alpha-methyl tyrosine: Comparison with PET, ^{124}IMT and first clinical results. *J Nucl Med* 1990;31:281–286.

15. Snook DE, Rowlinson-Busza G, Sharma HL, Epenetos AA. Preparation and in vivo study of iodine-124-labeled monoclonal antibody HE17E2 in a human tumour xenograft model: a prelude to positron emission tomography (PET). *Br J Cancer* 1990;62(suppl 10):89–91.

16. Wilson CB, Snook DE, Dhokia B, et al. Quantitative measurement of monoclonal antibody distribution and blood flow using positron emission tomography and ^{124}I in patients with breast cancer. *Int J Cancer* 1991;47:344–347.

17. Westera G, Reist HW, Buchegger F, et al. Radioimmuno positron emission tomography with monoclonal antibodies: a new approach to quantifying in vivo tumour concentration and biodistribution for radioimmunotherapy. *Nucl Med Commun* 1991; 12:429–437.

18. Larson SM, Pentlow KS, Volkow ND, et al. PET scanning of ^{124}I 3F8 as a novel approach to tumor dosimetry during treatment planning for radioimmunotherapy in a child with neuroblastoma. *J Nucl Med* 1992;33:2020–2023.

19. Bakir MA, Eccles SA, Babich JW, et al. c-erbB2 protein overexpression in breast cancer as a target for PET using iodine-124-labeled monoclonal antibodies. *J Nucl Med* 1992;33:2154–2160; 1993;34:290 [Erratum].

20. Rubin SC, Kairemo KJA, Brownell AL, et al. High-resolution positron emission tomography of human ovarian cancer in nude rats using ^{124}I-labeled monoclonal antibodies. *Gynecol Oncol* 1993;48:61–67.

21. Daghighian FD, Pentlow KS, Larson SM, et al. Development of a method to measure kinetics of radiolabeled monoclonal antibody in human tumor with applications to microdosimetry: positron emission tomography studies of iodine-124-labeled 3F8 monoclonal antibody in glioma. *Eur J Nucl Med* 1993;20:402–409.

22. Pentlow KS, Graham MC, Lambrecht RM, Cheung N-KV, Larson SM. Quantitative imaging of I-124 using positron emission tomography with applications to radioimmunodiagnosis and radioimmunotherapy. *Med Phys* 1991;18:357–366.

23. Kearfott K, Carroll LR. Evaluation of the performance characteristics of the PC4600 positron emission tomograph. *J Comput Assist Tomogr* 1984;8:502–513.

24. Batchelor S, Blake GM, Saunders JE. A comparison of three commercially available PET imaging systems. *Nucl Med Commun* 1992;13:20–27.

25. Lewellen TK, Bice AN, Harrison RL, Pencke MD, Link JM. Performance measurements of the SP3000/UW time-of-flight positron emission tomograph. *IEEE Trans Nucl Sci* 1988;NS-35:665–669.

26. Spinks TJ, Jones T, Gilardi MC, Heather JD. Physical performance of the latest generation of commercial positron scanner. *IEEE Trans Nucl Sci* 1988;NS-35:721–725.

27. Clem RG, Lambrecht RM. Enriched ^{124}Te targets for production of ^{123}I and ^{124}I. *Nucl Instrum Meth Phys Res* 1991;A303:115–118.

28. Bigler RE, Yoshizumi T, Graham MC. Positron instrumentation: intercomparison measurements, specifications, test procedure, figure of merit optimization, scatter measurements. In: Rao DV, Chandra R, Graham MC, eds. *Physics of nuclear medicine: recent advances, medical physics monograph no. 10*. New York: American Association of Physicists in Medicine; 1984:411–441.

29. Hoffman EJ, Huang SC, Phelps MJ. Quantitation in positron emission computed tomography: effect of object size. *J Comput Assist Tomogr* 1979;3:299–308.

30. Kessler RM, Ellis JR, Eden M. Analysis of emission tomographic scan data: limitations imposed by resolution and background. *J Comput Assist Tomogr* 1984;8:514–522.

31. Spinks TJ, Guzzardi R, Bellina CR. Performance characteristics of a whole-body positron tomograph. *J Nucl Med* 1988;29:1833–1841.

32. Hoffman EJ, Huang SC, Phelps ME, Kuhl DE. Quantitation in positron emission computed tomography: 4: effect of accidental coincidences. *J Comput Assist Tomogr* 1981;5:391–400.

33. Snyder WS, Ford MR, Warner GG, Watson SB. "S," Absorbed dose per unit cumulated activity for selected radionuclides and organs. *MIRD Pamphlet No. 11.* New York: Society of Nuclear Medicine; 1975.

34. Berman M, Braverman LE, Burke J, DeGroot L, McCormack KR, Oddie TH, Rohrer RH, Wellman HN, Smith EM. MIRD/dose estimate report no. 5: summary of current radiation dose estimates to humans from ^{123}I, ^{124}I, ^{125}I, ^{126}I, ^{130}I, ^{131}I, ^{132}I as sodium iodide. *J Nucl Med* 1975;16:857–860.

Stereotactic Coordinates from ECT Sinograms for Radionuclide-Guided Breast Biopsy

Raymond R. Raylman, Edward P. Ficaro and Richard L. Wahl

Department of Internal Medicine and Division of Nuclear Medicine, Department of Radiology, University of Michigan Medical Center, Ann Arbor, Michigan

Raw data from emission scanners contained in ECT sinograms can provide an abundance of information about the position of an object in the camera's field-of-view. Since some cancers can be detected by PET and SPECT which are not seen clearly on mammograms, CT or other scans, sinogram data could potentially be used to guide tumor biopsy. For example, positron-emitting (^{18}F-labeled Fluorodeoxyglucose) and single-photon emitting (^{99m}Tc-labeled-sestamibi) radiopharmaceuticals have been used successfully to detect many types of breast cancer. By utilizing some relatively simple geometric relationships, a sinogram-based method for biopsy of radiopharmaceutical-avid breast masses guided by data from PET and SPECT scanners has been developed and validated in phantom studies. **Methods:** A pair of projection views from a series of sinograms is used to calculate the position of photon-emitting objects. Calculated positions of spheres ranging in size from 1.6 to 3.4 cm diameters containing ^{18}F and ^{99m}Tc were compared with measured positions. By adding a single radioactive fiducial marker, emission-guided biopsy of simulated breast lesions was performed with a specially designed phantom containing photon-emitting spheres 12.7 mm in diameter. **Results:** Correlation between calculated and measured object coordinates were excellent (R = 1.0, R = 1.0 and R = 0.998; x, y and z coordinates, respectively). The maximum error in localization was ±3 mm. One hundred percent (10 of 10) of the attempted biopsies of simulated tumors were successful. **Conclusion:** A method for rapidly determining the position of photon-emitting objects in an emission scanner has been developed and tested. This technique, which does not require standard emission or anatomic images, could be used with dedicated biopsy machines or incorporated into "add-on" biopsy devices for existing PET or SPECT cameras.

Key Words: fluorine-18-FDG; technetium-99m-sestamibi; stereotactic biopsy; needle biopsy; breast cancer; emission computed tomography

Sinograms obtained during standard ECT (PET and SPECT) data acquisitions contain abundant information about the location of areas of increased tracer uptake. We have developed a technique that uses data contained in sinograms to rapidly calculate the three-dimensional position of any radiopharmaceutical-avid site in the field-of-view of an emission scanner, without image reconstruction or co-registration with an anatomical image. An object in a tomograph can be characterized by its radius, angular and axial position. These coordinates are transformed by the scanning process to data that gives the position of the point in terms of its distance from the center of projections acquired at numerous angles relative to the scanner reference frame ("sinogram space"). Utilizing two of these views from each sinogram in a set of sinograms (one sinogram is acquired for each image plane), the object's position can be transformed back into the cylindrical coordinate system of the scanner.

Recently, the use of radiotracers to detect breast cancers has met with considerable interest and success. Wahl and others (1–6) have shown that [^{18}F]fluorodeoxyglucose (FDG) PET is very sensitive for detecting many breast cancers. In addition, Khalkhali and others (7–9) have reported that ^{99m}Tc-sestamibi scintimammography has improved specificity and sensitivity for detecting and evaluating breast tumors compared to standard mammography. Both radiopharmaceutical methods are sensitive to the presence of metabolically active lesions and are potentially able to detect malignant tumors otherwise invisible to mammography. The needle or core biopsy of lesions visible only with radiotracers presents a significant challenge, since most biopsies are guided by techniques that rely upon tissue density contrast [e.g., MRI (10,11), mammography (12–14) and ultrasound (15–17)]. Therefore, we propose the application of PET and SPECT sinogram-derived stereotactic coordinates for the guidance of breast tumor biopsies. In both applications, the distance from a single fiducial marker could be rapidly calculated; in contrast to other stereotactic methods (18–20), such as the Brown-Roberts-Wells technique (18), which require numerous fiducial points and image reconstruction. In addition, transmission scans to provide attenuation correction maps may not be necessary in many cases. Since image reconstruction and attenuation correction are not required, this new method could considerably simplify spatial localization of tracer uptake detected with PET and SPECT systems.

MATERIALS AND METHODS

Emission scanners acquire line integrals (lines-of-response) of photon emissions originating from within the field of view. For each image plane, data are stored in a two-dimensional array where each row denotes the angle at which the detector array was positioned and each element within a row contains the number of events detected by an individual detector within an array of detectors. Figure 1 is a schematic drawing of the geometrical relationship between an object and a detector array in an emission scanner. The scanning process transforms the position of a photon-emitting object from cylindrical coordinates (R and φ) into the "sinogram space" coordinates L and θ. This transformation can be expressed by the equation:

$$L = R \cdot \sin(\varphi - \theta). \qquad \text{Eq. 1}$$

The parameter L is the distance from the center of the detector array to the line integral of photons detected from the object; θ is the angular position of the detector array.

Calculation of Three-Dimensional Coordinates

Given a set of sinograms and Equation 1, it is possible to calculate the position of an object in the scanner coordinate reference frame. This calculation requires data from two views. By
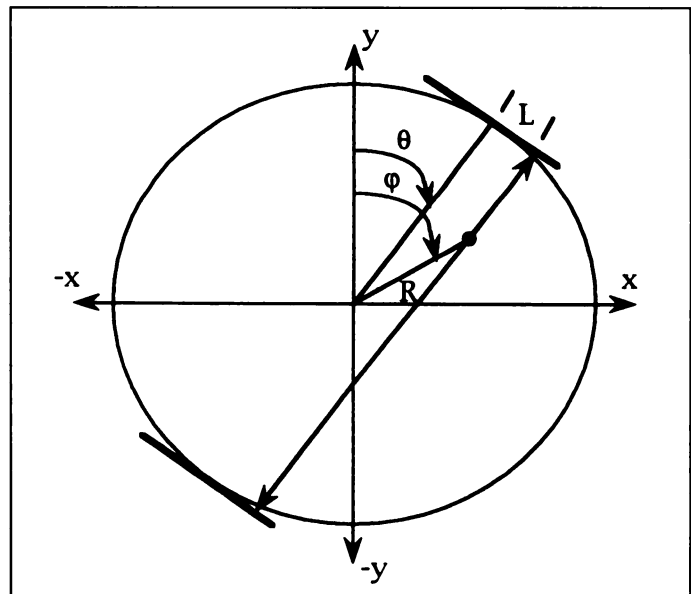

FIGURE 1. Schematic diagram of the transformation from "scanner space" into "sinogram space" in a PET scanner. A photon-emitting object at a radius R and angle φ is shown in a scanner. This object is viewed by a detector array located at an angle θ.

selecting data acquired at angles of $\theta = 0°$ and γ from a sinogram we can re-write Equation 1 as

$$L_1 = R \cdot \sin \varphi; \; [\theta = 0°] \qquad \text{Eq. 2}$$

and

$$L_2 = R \cdot \sin(\varphi - \gamma)$$

$$= R \cdot [(\sin \varphi \cdot \cos \gamma) - (\cos \varphi \cdot \sin \gamma)]; \; [\theta = \gamma] \qquad \text{Eq. 3}$$

in which L_1 is the distance from the line integral sampling the photon flux from the object to the center of the detector array positioned at a rotation angle $\theta = 0°$, and L_2 is the distance from the line integral to the center of the detector array at a rotation angle $\theta = \gamma$. Equation 3 was cast into a more useful form by insertion of the trigonometric identity for $\sin(\varphi - \gamma)$. Dividing Equation 3 by Equation 2 we obtain

$$\frac{L_2}{L_1} = \cos \gamma - \cot \varphi \cdot \sin \gamma. \qquad \text{Eq. 4}$$

Since the distances L_1 and L_2 can be obtained from the sinograms and γ is given, Equation 4 can be solved for the angular position of the object in the scanner (φ). The object's distance from the center of the scanner (R) can then be calculated from Equation 2. The x- and y-coordinates of the object in the scanner reference frame are given by: $x = R \cdot \sin \varphi$ and $y = R \cdot \cos \varphi$. The z-coordinate is determined by first locating the detector plane which sampled the center of the object, and then, given the spacing between planes, calculating the axial distance from the top plane of the scanner to the object.

Photons reaching two detector arrays at different rotation angles can pass through widely varying amounts and types of attenuating material; such as is encountered in the upper torso. Since the application of attenuation correction is not desired (to minimize acquisition and processing time), there will probably be vastly unequal image intensities between the two views. One way to reduce this problem is to choose a view angle (γ) very close to 0°. This procedure, however, limits the range of angles at which equivalent intensities can be obtained. An alternative method is to select two views that are symmetric about the y-axis ($\pm\gamma$). Thus,
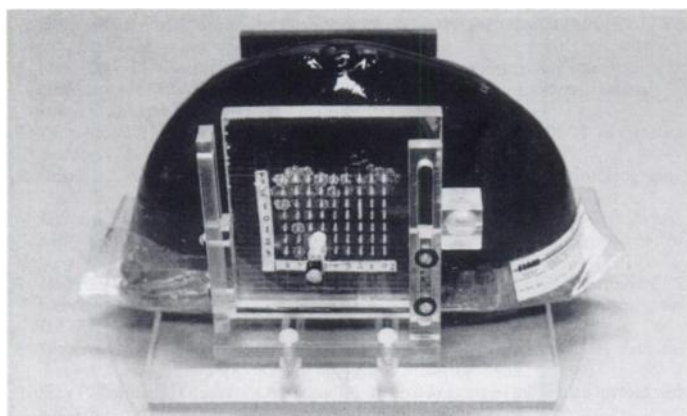
FIGURE 2. Prototype emission-guided breast tumor biopsy device. This device consists of a single fiducial marker and compression paddles with small needle guide holes (5 mm apart) in one of the paddles. Also shown is the compressed breast phantom with its long-axis extending from left to right.

the types and total amounts of tissue traversed by the photons are more balanced for the two sets of data, thereby facilitating the localization of the centroid of the object in both views.

When symmetric view angles are employed, the original x-y coordinate axis is rotated by the angle $-\gamma$ to a new coordinate system x'-y'. In this system, L_1 and L_2 retain their previous definitions, while the total view angle (γ) becomes 2γ. Therefore, Equation 2 remains the same and Equation 4 becomes:

$$\frac{L_2}{L_1} = \cos 2\gamma - \cot \varphi' \cdot \sin 2\gamma. \qquad \text{Eq. 5}$$

From Equations 5 and 2, the position of the object in the rotated reference frame (R' and φ') is determined, allowing calculation of x' and y'. The z-coordinate is calculated as previously described. A transformation back to the unrotated scanner coordinates is then applied to obtain the position of the object in the scanner.

Analysis Software

The software used to calculate the three-dimensional coordinates was written in IDL (Interactive Data Language; RSI, Boulder CO). The name of the sinogram file, name of the normalization file (in the case of PET scans) and view angle are supplied by the user. In the current version of the software, the appropriate projections from 15 sinograms for each of the specified two views acquired on a Siemens ECAT 931 PET scanner (Hoffman Estates, IL) are extracted. These projections are determined by the view angle and angular sampling frequency of the scanner. To reduce the effects of statistical noise, five projections for each of the two view angles are summed. A Hamming filter (frequency cutoff = 1.2 cycles/cm) is applied to the summed projections in order to enhance tumor contrast.

Since the spacing between lines-of-response for a Siemens ECAT 931 is 3.13 mm and the spacing between image planes is 6.74 mm, data from adjacent image planes were interpolated to obtain equivalent ray spacing in all directions. A linear interpolation algorithm was used to create a new dataset that expanded the 15 planes to 29. Thus, each composite view is stored in a 192 × 29 matrix; where the transaxial pixel spacing is 3.13 mm and axial spacing is 3.37 mm. An alternate approach would be to interleave two sets of sinograms acquired with a 3.37 mm axial separation; however, this would increase the time required for the procedure. Data acquired with a Picker Prism XP3000 SPECT scanner were stored in a 128 × 29 matrix; no interpolation was necessary because axial and transaxial pixel spacing was uniform (3.56 mm).

Experimental Validation

To accurately calculate the position of objects utilizing this method, a validation experiment was performed. Four hollow
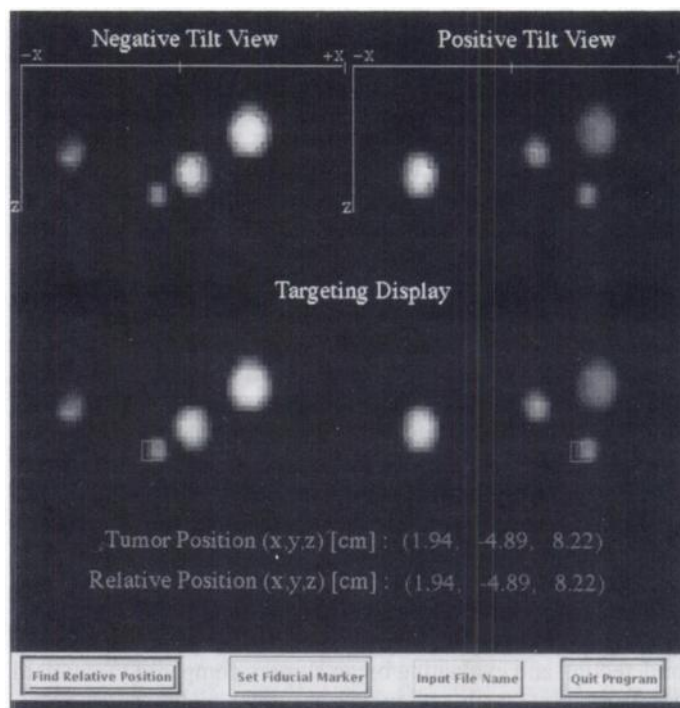

FIGURE 3. User display from the stereotactic software showing an image of four spheres filled with [18F] in an elliptical tank (view angle = 75°). The center of mass of the tumor is marked with an 'x'. The box delineates the extent of the search area.

spheres (diameters ranging from 1.6 to 3.4 cm) containing [18F] (concentration = 222 kBq/ml) were positioned at unique locations inside a large elliptical tank filled with water. The phantom was then carefully positioned in a Siemens ECAT 931 PET scanner and a 15-min static PET acquisition was performed. No attenuation or scatter corrections were applied. The same phantom was used to test the ability of this method to locate areas of increased single-photon emitting radiopharmaceutical uptake. The four spheres were filled with [99mTc] (222 kBq/ml). Data were acquired using a Picker Prism 3000XP triple-head SPECT scanner. Due to scanner software limitations, a 360° step and shoot acquisition was performed (30 seconds per stop, each head moved 120°), each view was acquired at 1° increments. Following the data acquisition, sinograms were utilized, as previously described, to calculate the Cartesian coordinates of each sphere. Data from five independent measurements were used to calculate the mean position of the spheres. These results were then compared to the known locations.

Emission-Guided Needle Biopsy

Our technique for calculation of three-dimensional coordinates could facilitate biopsies of [18F]FDG or [99mTc]-sestamibi-avid lesions. To test this proposition, a small breast compression fixture was constructed (Figure 2). A compressed breast with lesions was simulated using a specially manufactured phantom (Gammex/RMI; Madison WI). This phantom contains hollow regions that can be filled with radiopharmaceuticals (the phantom is shown in Figure 2). The lesions are approximately 1 cm in diameter and contained FDG concentrations equivalent to standard uptake values (SUVs) ranging from 1 to 7 (assuming a 370-MBq injection of FDG and a 70-kg patient). These values span the lower range of SUVs reported for FDG in human breast cancer 1 hr following infusion (5). The long-axis of the simulated compressed breast phantom (the long-axis of the compressed breast is perpendicular to the direction of compression as illustrated in Figure 2) mounted in the biopsy device was aligned with the axis of the ECAT 931 PET scanner. A 10-min static acquisition was performed and the sinograms used to calculate the positions of the fiducial marker and
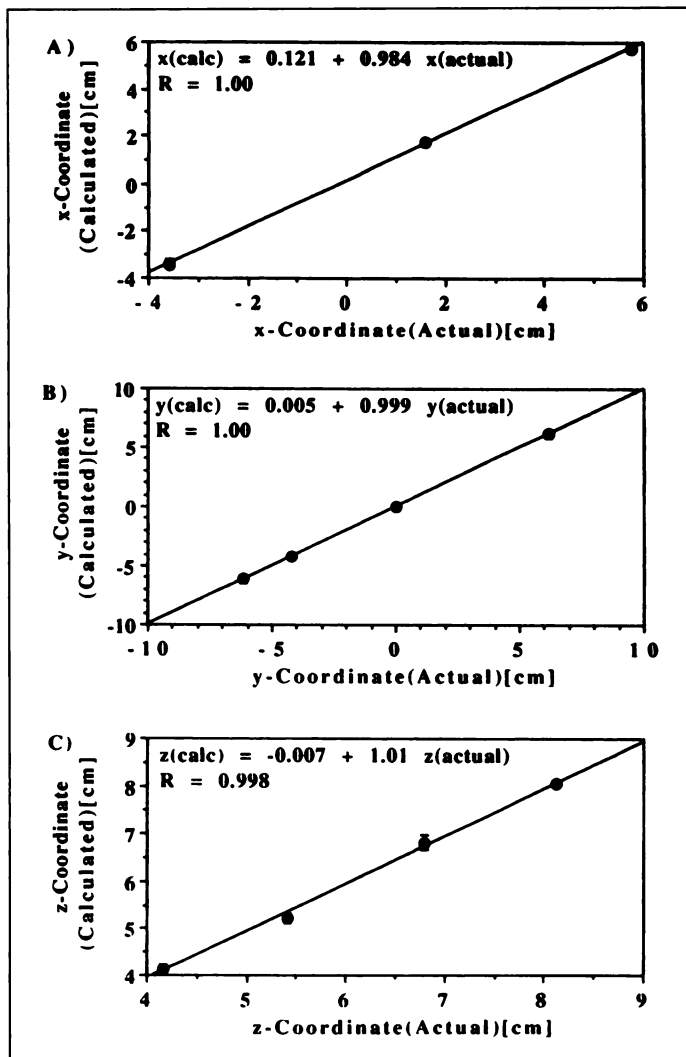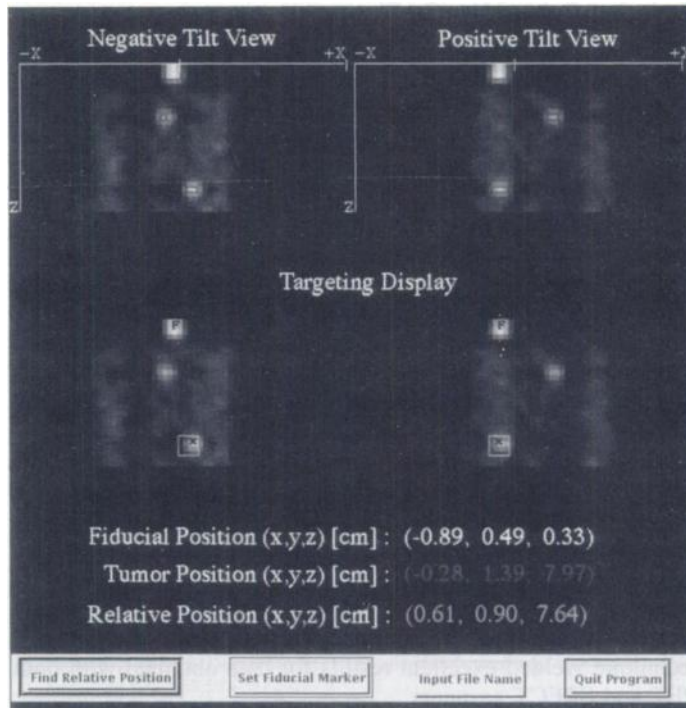
FIGURE 5. Stereotactic image of the compressed breast phantom containing background activity (view angle = 80°). The symbols on the display are the same as those shown in Figure 3. The fiducial marker is visible at the top of the images and is marked by the letter 'F'. Note the relatively uniform intensity of the simulated tumors in the two symmetric views.

FIGURE 4. Comparisons of calculated (mean ± s.d.) versus known positions of spheres filled with ^{18}F. The results of fits with a straight line are shown.

lesion. From the calculated positions of the fiducial marker and the simulated tumor, the software determined the proper needle guide hole and necessary needle insertion depth. Calculation of the proper needle positioning requires approximately 1 min of operator time.

It was not possible for this study to manufacture a biopsy phantom that could simulate the tracer uptake of surrounding normal breast tissue. To address this issue, another phantom was constructed. This phantom consists of a 3 × 9 × 10 cm tank (representative of a large compressed breast) containing two hollow spheres (1.27 cm diameter) that could be filled with photon-emitting radionuclides. Additionally, a third sphere was attached to the exterior of the tank to serve as a fiducial marker. To simulate tumor contrast in a typical breast biopsy, the spheres were filled with ^{18}F (37 kBq/ml; SUV = 7 for a 370-MBq injection and a 70-kg patient). The tank was filled with a solution containing ^{18}F (4.63 kBq/ml; SUV = 0.875 for a 370-MBq FDG injection and a 70-kg patient). Thus, a tumor-to-background ratio of 8:1 was achieved, which is reasonably typical of FDG contrast 1 hr postinjection in human studies (5). Again, the long-axis of the phantom was coaxial with the axis of the scanner. A 15-min data acquisition with no attenuation correction was performed. Positions of the two simulated lesions relative to the fiducial marker were determined and compared to the known relative tumor locations. This phantom was also filled with appropriate amounts of ^{99m}Tc to obtain a tumor-to-background ratio of 4, which is in the upper part

of the range of values reported in humans by Khalkhali et al. (21), to test the ability to locate ^{99m}Tc-sestamibi-avid breast tumors.

RESULTS

Experimental Validation

Figure 3 shows the display produced by the stereotactic software. In this example, a water-filled phantom holding four spheres of varying size containing ^{18}F was imaged. The user is prompted to select the center of the object (in both views) whose position must be calculated. The software then uses data from within a 6 × 6 pixel search area surrounding this point to calculate the center of mass of counts within this region. The coordinates of the object are then calculated and displayed. Note the relatively uniform image intensities of the spheres in the two views; although the effects of increased attenuation of the deepest objects are apparent.

Results from the validation experiment are shown in the plots of Figure 4. Note the excellent correlation between the calculated and actual values. Lines fit to the data have slopes ranging from 0.984 to 1.01 and R-values ranging from 0.998 to 1.0. The largest y-axis intercept was 1.21 mm, calculated for the x-coordinate. Data for the x-coordinate also produced the slope with the largest deviation from unity (0.984). These small errors are probably due to a minor error in positioning of the phantom in the scanner. The greatest standard deviation calculated for the coordinates of the spheres was 3.3 mm. The plot displaying the x-coordinate data appears to have only 3 points. Actually, two spheres had identical x-coordinates (−4.3 cm) and their data points are plotted very closely together. Similar results were obtained from data acquired with a Picker Prism 3000XP SPECT scanner with the spheres filled with ^{99m}Tc. The spheres located deepest in the phantom were much more difficult to detect due to the increased attenuation of the 140-keV gamma rays compared to the 511-keV annihilation photons.

Emission-Guided Needle Biopsy

In all of the simulated breast tumor biopsies (n = 10), the needle successfully penetrated the sham lesions and 90% of the liquid was withdrawn from the spheres. It is important to note that all simulated biopsies were performed using coordinates calculated from the sinogram-based method; no visual guidance of the biopsy needle was utilized. Figure 5 shows the images obtained of the breast phantom with simulated normal tissue background. To confirm the ability to biopsy these "tumors," their positions relative to the fiducial marker were calculated. Relative coordinates determined from a PET scan for sphere I are: 1.77 cm, −3.05 cm, 2.90 cm, and for sphere II: 0.61 cm, 0.90 cm, 7.64 cm. Using a SPECT camera, the relative position of sphere I was calculated to be: 1.77 cm, −3.19 cm, 2.87 cm, while sphere II's position was calculated to be: 0.79 cm, 0.77 cm, 7.54 cm. The actual coordinates measured from the phantom for sphere I are: 1.61 cm, −3.19 cm, 2.96 cm, and the actual coordinates for sphere II are: 0.65 cm, 0.82 cm, 7.75 cm. Errors present in the positions of the fiducial mark and tumors propagate to create the errors in calculations of relative position. It is apparent, however, that this process does not significantly affect localization of the simulated lesions. Application of this technique yielded excellent results for data obtained with both PET and SPECT scanners.

DISCUSSION

The wealth of information contained in emission tomography sinograms is often overlooked. This raw data contains potentially useful information about the physical location of objects in the scanner's field-of-view. It is possible to accurately determine the position of virtually any photon-emitting object present in the scanner through some relatively simple geometrical manipulations of sinogram data. All that is required are two views from a set of sinograms. The results shown in Figure 4 demonstrate the high degree of accuracy in locating the position of photon-emitting objects attainable with this method.

The capability to perform biopsies of lesions utilizing photon-emission guidance will be required as imaging methods based on tumor-avid tracers labeled with single photon or positron-emitting radionuclides continue to emerge. The imaging of breast cancers with radiopharmaceuticals has been successful. Therefore, it was reasonable to first apply this technique to the needle biopsy of breast lesions detected with emission scanners (e.g., PET and SPECT). Experiments utilizing simulated breast lesions indicated that this procedure is able to reliably guide the placement of biopsy needles. One-centimeter diameter capsules containing varying amounts of ^{18}F (simulating the uptake of FDG in human breast cancers) were successfully detected and "biopsied." The relatively good precision of this method (maximum ±3.3 mm) should allow for the biopsy of most tumors in the clinically relevant range, especially if multisample biopsies are performed. Clearly, the precise localization of very small tumors will be difficult. Although the smallest object imaged in this investigation was 12.7 mm in diameter, it should be possible to localize smaller tumors. For example, Mena et al. (22) have used scintigraphic localization using two orthogonal views and photon-emitting reference lines placed along the x-, y- and z-axis to guide the "biopsy" of simulated breast tumors as small as 3 mm. Size limits of tumors that can be effectively sampled with the stereotactic method are largely determined by the resolution of the scanner employed and the tumor-to-background contrast.

Since the breast biopsy phantom did not simulate the background radiation present in normal breast tissue, an additional phantom with the approximate dimensions of a compressed breast was employed. The PET-guided biopsy display, shown in Figure 5, demonstrates that, given proper choice of view angles, the simulated tumors are clearly detectable, even in the presence of background activity. Reduction of photon attenuation effects and scatter from myocardial uptake can be accomplished by choosing a large view angle. At these angles, photons that reach the detector array have traversed a minimum of breast and upper torso tissue. In addition, viewed at these angles, images of the myocardium and breast areas in most patients will not overlap. Contamination of the signal from breast tumors due to myocardial activity, therefore, is minimized, which is especially important for Sestamibi- and FDG-guided biopsies. As our results demonstrate, these angles still allow accurate stereotactic calculation of lesion positions.

Large view angles also aid in increasing the tumor-to-background contrast. This effect is related to the fact that the individual elements in a sinogram are the results of an integral along the detectors' lines-of-response. We envision that breast compression would be applied perpendicular to the long-axis of the body; hence the long-axis of the compressed breast is co-axial with the long-axis of the body. Therefore, if the patient is placed on a standard scanning bed, the long-axis of the compressed breast is aligned with the axis of the scanner. In this orientation, compression of the breast, in addition to stabilizing the breast during biopsy, reduces the effective thickness of the breast in the transaxial plane. Hence, the detector response ray-lengths through the compressed breast is lessened and are minimized at angles close to 90° (angles of 0° and 90° cannot be used in this method to calculate stereotactic coordinates). Two effects emerge as the intersection lengths are reduced. First, for detectors sampling signals from tumors, the fractional contribution of tumor to the line integrals is increased. Second, for detectors sampling normal tissue, the amplitude of the line integrals is reduced. Both effects increase the contrast between tumor and normal tissue by reducing the amplitude of background activity included in the dataset. Since the algorithm for calculation of object position performs relatively well at most view angles (except at angles close to 0° and 90°), the optimal view angle is the one at which the best tumor-to-background contrast occurs. This angle can vary depending upon the patient's physiology and anatomy.

While excellent results were obtained from data acquired in measurements utilizing ^{99m}Tc, the higher absorption of the relatively low-energy photons emitted by many single-photon emitting radionuclides require special considerations (e.g., ^{201}Tl). In patients with tumors deep inside the body, it may be necessary to use attenuation corrections. The increased attenuation is, to a certain extent, advantageous when performing breast biopsies. The flux of background gamma rays emanating from the myocardium and other relatively deep structures is reduced by attenuation. While attenuation will also reduce the gamma ray flux from tumors, axial compression of the breast lessens this effect by reducing the amount of tissue traversed by transaxially directed gamma rays before exiting the breast.

Only two views of the breast are required to calculate lesion position. This procedure can therefore be performed not only with PET and SPECT cameras, but it should also work with a single-head gamma camera (including cameras fitted with 511 keV collimators). Indeed, the use of a gamma camera may be more efficient, since only the necessary views need be acquired and the detectors can be placed very close to the breast. Dedicated needle biopsy machines possessing a small number of high-resolution detectors could be constructed at a fraction of the cost of a PET or SPECT system. For example, the positron emission mammography device proposed by Thompson et al.

(23) could be used in conjunction with this method to guide core biopsies of breast masses. Or, a separate removable device that can be fixed to a PET, SPECT or gamma camera bed could be fabricated. The latter approach would enable these pre-existing devices to be temporarily converted to emission-guided biopsy machines.

CONCLUSION

A simple method for calculation of the position of radionuclide-avid tumors or other photon-emitting bodies utilizing two views from tomograph sinograms has been proposed and experimentally validated. This method has been used to accurately and precisely calculate the position of spheres containing either single-photon or positron-emitting radionuclides. Furthermore, the biopsy of simulated radiopharmaceutical-avid breast lesions was investigated and proven feasible. The excellent results obtained from these experiments indicate that future clinical evaluation of this biopsy method are warranted, especially in situations where anatomical imaging methods are unrevealing.

REFERENCES

1. Wahl RL, Hutchins GD, Buchsbaum DJ, et al. Fluorine-18-2-deoxy-2-glucose uptake into human tumor xenografts. Cancer 1991;67:1545–1550.
2. Wahl RL, Cody RL, Hutchins GD, Mudgett EE. Primary and metastatic breast carcinoma: initial clinical evaluation with PET with radiolabeled glucose analog 2-[18F]-fluoro-2-deoxy-d-glucose. Radiology 1991;179:765–770.
3. Tse NY, Hoh CK, Hawkins RA, et al. The application of positron emission tomography imaging with fluoro-deoxyglucose to the evaluation of breast disease. Ann Surgery 1992;216(1):27–34.
4. Niewig OE, Kim EE, Wong W-H, et al. Positron emission tomography with fluorine-18-deoxyglucose in the detection and staging of breast cancer. Cancer 1993;71:3920–3925.
5. Adler LP, Crowe JJ, Al-Kaise NK, Sunshine JL. Evaluation of breast masses and axillary lymph nodes with [18F]2-deoxy-2-fluoro-d-glucose. Radiology 1993;187:743–750.
6. Wahl RL, Helvie MA, Chang AE, Andersson I. Detection of breast cancer in women after augmentation mammoplasty using fluorine-18-fluorodeoxyglucose PET. J Nucl Med 1994;35:872–875.
7. Khalkhali I, Mena I, Diggles L. Review of imaging technique for the diagnosis of breast cancer: a new role of prone scintimammography using technetium-99m-sestamibi. Eur J Nucl Med 1994;21:357–362.
8. Kao CH, Wang SJ, Liu TJ. The use of technetium-99m-methoxyisobutylisonitrile breast scintigraphy to evaluate palpable breast masses. Eur J Nuc Med 1994;21:432–436.
9. Khalkhali I, Mena I, Jouanne E, et al. Prone scintimammography in patients with suspicion of carcinoma of the breast. J Am Coll Surg 1994;178:491–497.
10. Heywang-Köbrunner SH. Contrast-enhanced MRI of the breast. New York: Basel; 1990.
11. Heywang-Köbrunner SH, Huynh AT, Vichweng P, et al. Prototype breast coil for MR-guided needle localization. J Comp Assist Tomogr 1994;18:876–881.
12. Dowlatshahi K, Gent HJ, Schmidt R, Jokich PM, Bibbo M, Sprenger E. Nonpalpable breast tumors: diagnosis with stereotaxic localization and fine-needle aspiration. Radiology 1989;170:427–433.
13. Parker SH, Lovin JD, Jobe WE, et al. Stereotaxic breast biopsy with a biopsy gun. Radiology 1990;176:741–747.
14. Sullivan DC. Needle core biopsy of mammographic lesions. Am J Roentgenol 1994;162:601–608.
15. Fornage BD, Sneige N, Faroux MJ, Andry E. Sonographic appearance of and ultrasound-guided fine-needle aspiration biopsy of breast carcinoma smaller than 1 cm³. J Ultrasound Med 1990;9:559–568.
16. Parker SH, Jobe WE, Dennis MA, et al. US-guided automated large-core breast biopsy. Radiology 1993;187:507–511.
17. Sneige N, Fornage BD, Saleh G. Ultrasound-guided fine-needle aspiration of nonpalpable breast lesions. Am J Clin Pathol 1994;102:98–101.
18. Saw CB, Ayyongan K, Suntharalingan S. Coordinate transformations and calculation of the angular and depth parameters for a stereotactic system. Med Phys 1987;14:1042–1044.
19. Levivier M, Goldman S, Bidaut L, et al. Positron emission tomography-guided stereotactic brain biopsy. Neurosurgery 1992;31:792–797.
20. Alexander III E, Loeffler JS, Schwartz RB, et al. Thallium-201, technetium-99m-HMPAO SPECT imaging for guiding stereotactic craniostomes in heavily irradiated malignant glioma patients. Acta Neurochir (Wien) 1993;122:215–217.
21. Khalkhali I, Cutrone J, Mena I, et al. Technetium-99m-sestamibi scintimammography of breast lesions: clinical and pathological follow-up. J Nucl Med 1995;36:1784–1789.
22. Mena F, Mena I, Diggles L. Design and assessment of scintigraphy guided stereotaxic localization techniques of breast tumors. J Nucl Med 1994;35:62P (abstract).
23. Thompson CJ, Murthy K, Weinberg IN, Mako F. Feasibility study for positron emission mammography. Med Phys 1994;21:529–538.

Three-Dimensional Bone Scintigraphy Using Volume-Rendering Technique and SPECT

Toyotsugu Ota, Itsuo Yamamoto, Hideo Ohnishi, Itsuaki Yuh, Yusuke Kigami, Teruyasu Suzuki, Yasuyo Yamamura, Kiyoshi Murata and Rikushi Morita

Department of Radiology, Shiga University of Medical Science, Seta, Otsu, Shiga, Japan

Three-dimensional bone scintigraphic images were made and their usefulness and limitations discussed. **Methods:** After usual bone scan procedures, single-photon emission computed tomography (SPECT) data were taken and reconstructed into three-dimensional images. Volume rendering methods were used. **Results:** Three cases of three-dimensional bone scintigraphy were obtained; one of a normal patient, one of a case of transplanted kidney and incomplete fracture of the left femoral head, and one of a case of degenerative joint disease (DJD) on the left temporomandibular joint (TMJ). The three-dimensional structure of the skeletal system was depicted more clearly by the three-dimensional images than by a conventional bone scan. **Conclusion:** Three-dimensional bone scintigraphs were thought to provide additional information for better understanding of the nature of bone lesions. Some technical improvements including automated threshold level determination and feature extraction for detecting abnormal high uptake are required before routine use can be envisaged.

Key Words: three-dimensional imaging; bone scintigraphy; SPECT; volume rendering

Recently, reconstruction techniques for three-dimensional imaging have made remarkable progress and are being applied to various modalities, such as CT, MRI and some scintigraphies. Some of them are already being utilized in bedside